Received: 30 June 2023 | Revised: 10 November 2023 | Accepted: 5 December 2023

DOI: 10.1002/pip.3768

SPECIAL ISSUE ARTICLE

PROGRESS IN PHOTOVOLTAICS WILEY

Electron contact interlayers for low-temperature-processed crystalline silicon solar cells

Jesus Ibarra Michel[1,2] | Anh Huy Tuan Le[3] | Di Yan[1] | Willem-Jan Berghuis[4] | Lars Korte[2] | Anyao Liu[5] | Sieu Pheng Phang[5] | Wenhao Chen[6] | Daniel Macdonald[5] | Bart Macco[4] | Ziv Hameiri[3] | James Bullock[1]

[1]Department of Electrical and Electronic Engineering, The University of Melbourne, Melbourne, Australia

[2]Department Perovskite Tandem Solar Cells, Helmholtz-Zentrum Berlin, Berlin, Germany

[3]School of Photovoltaic and Renewable Energy Engineering, University of New South Wales, Kensington, Australia

[4]Department of Applied Physics, Eindhoven University of Technology, Eindhoven, MB, The Netherlands

[5]School of Engineering, College of Engineering, Computing and Cybernetics, The Australian National University, Canberra, ACT, Australia

[6]School of Testing and Photoelectric Engineering, Nanchang Hangkong University, Nanchang, China

Correspondence

Jesus Ibarra Michel, Department Perovskite Tandem Solar Cells, Helmholtz-Zentrum Berlin, 12489 Berlin, Germany.
Email: jibarramiche@student.unimelb.edu.au

James Bullock, Department of Electrical and Electronic Engineering, The University of Melbourne, 3010, Australia.
Email: james.bullock@unimelb.edu.au

Funding information

Australian Renewable Energy Agency (ARENA), Grant/Award Number: RND013

Abstract

This study focuses on electron-selective passivating contacts for crystalline silicon (c-Si) solar cells where an interlayer is used to provide a low contact resistivity between the c-Si substrate and the metal electrode. These electron contact interlayers are used in combination with other passivating interlayers (e.g., a-Si:H, TiO_x, and Nb_2O_5) to improve surface passivation whilst still permitting contact resistivities suitable for high-efficiency solar cells. We show that a wide variety of thermally evaporated materials, most of which have ionic character, enable an Ohmic contact between n-type c-Si and Al. From this pool of compounds, we observed that CsBr has especially promising behavior because of its excellent performance and thermal stability when combined with thin passivating layers. With different test structures, we were able to demonstrate low contact resistance using TiO_x/CsBr, Nb_2O_5/CsBr, and a-Si:H/CsBr stacks on n-type c-Si. The quality of the provided surface passivation depended on the stack but we achieved the best overall passivation stability with TiO_x/CsBr. Finally, we were able to demonstrate an efficiency >20% on a laboratory-scale solar cell that implements the TiO_x/CsBr/Al stack as full-area rear-side electron selective contact.

KEYWORDS

electron selective contacts, passivating contacts, silicon solar cells

1 | INTRODUCTION

Hydrogenated amorphous silicon (a-Si:H) and polysilicon (poly-Si) based passivating contacts have taken the lead in achieving the highest efficiencies in crystalline silicon (c-Si) solar cells—being demonstrated above 26% in some cases.[1–4] Their success lies in their ability to achieve high open circuit voltages (V_{oc}) whilst maintaining sufficiently low specific contact resistivities (ρ_c) to not significantly reduce the cell's fill factor. However, both of these contact structures suffer from non-negligible parasitic absorption of light due to direct band-to-band excitation and free carrier

This article belongs to the WCPEC-8 Special issue published in issue 31:12 (WCPEC-8: Progress in Photovoltaics: Research and Applications: Vol 31, No 12).

absorption, predominantly in the doped layers.[5,6] To prevent parasitic absorption, other wider band gap materials, with the same ability to collect electrons and holes and/or passivate the silicon surface, have been tested as replacements in the contacted regions of solar cell devices.[7–13]

All of the electron contact demonstrations in high efficiency (i.e., >20%) c-Si solar cells consist of a stack of films, each with a different role, rather than a single layer. These systems are typically formed by one layer that provides passivation at the c-Si surface (i.e., passivating Si dangling bonds), in combination with another layer that promotes electron extraction from the c-Si. Examples of passivating materials employed in electron contacts are silicon dioxide (SiO_2), hydrogenated amorphous silicon (a-Si:H), and some transition metal oxides like titanium dioxide (TiO_x) and niobium oxide (Nb_2O_5).[8,9,14–16] Generally, these passivation layers do not provide sufficient electron selectivity on their own and are combined with a low work function electrode to enable electron collection. The low work function electrode is commonly achieved using a thin (<3 nm) and transparent interlayer, such as LiF, MgF_x, or MgO_x,[9–11] under the metal layer, reducing its work function. These work function-reducing interlayers are typically ionic on their own or tend to form dipoles at the interface with other materials.[17] Such approaches have already been demonstrated in laboratory-scale silicon cells achieving >23%.[8]

The use of thin ionic compound interlayers to improve electron injection and extraction has been a successful approach for organic-based semiconductor devices such as organic light emitting diodes and organic solar cells.[7,18,19] The mechanisms leading to enhanced electron contact performance in these systems are still under debate.[18–24] For silicon-based devices, thin insulating interlayers have been used to reduce Fermi-level pinning.[25–29] This would allow the low work function of the metal contact material, such as aluminum (Al), to have a larger impact on the bending of the c-Si bands. In addition, insulating layers that have a strong ionic character have been suggested to aid in the formation of a work function-reducing dipole at metal surfaces.[17] A dipole could be formed by either charge transfer between the metal and the corresponding ionic material or physically by Pauli repulsion for very ionic interfacial layers.[30] Others have suggested that dissociation of the ionic metal compounds occurs after deposition, which could lead to low-work function metal ions being left at the interface or diffusing into the semiconductor substrate and doping it.[21] In device-relevant layer stacks, it is possible that multiple mechanisms take place at the same time, depending on the exact compound and the interacting layers. In any case, the end result of a low work function layer forming on top of c-Si is a larger electron population at the surface, which in turn improves the electron selectivity.[31]

We emphasize that most of the metal compound interlayers that have been used to improve electron collection in c-Si have either a low work function parent metal as the cation, a highly electronegative anion, or both. Due to the ionic characteristics of these materials, the formation of dipoles at the interface either with the c-Si substrate or the metal electrode likely plays an important role in reducing the work function and facilitating electron extraction. This is represented through a band diagram in Figure 1A. This schematic represents the formation of a work function-reducing dipole between an n-type c-Si substrate and a metal overlayer. Note that the polarity/alignment of the dipole is a key factor in determining whether the work function of the metal is reduced or increased. In this study, we explore and compile data for a large group of compounds, most of which are highly ionic by nature. These are all demonstrated to form Ohmic contacts on n-type c-Si. From this list of candidates, we then focus on CsBr, due to its ability to be combined with a range of passivating interlayers whilst maintaining contact resistivities which are applicable to high-efficiency c-Si solar cells. The most promising behavior is found for a TiO_x/CsBr/Al contact stack which, when applied as a full-

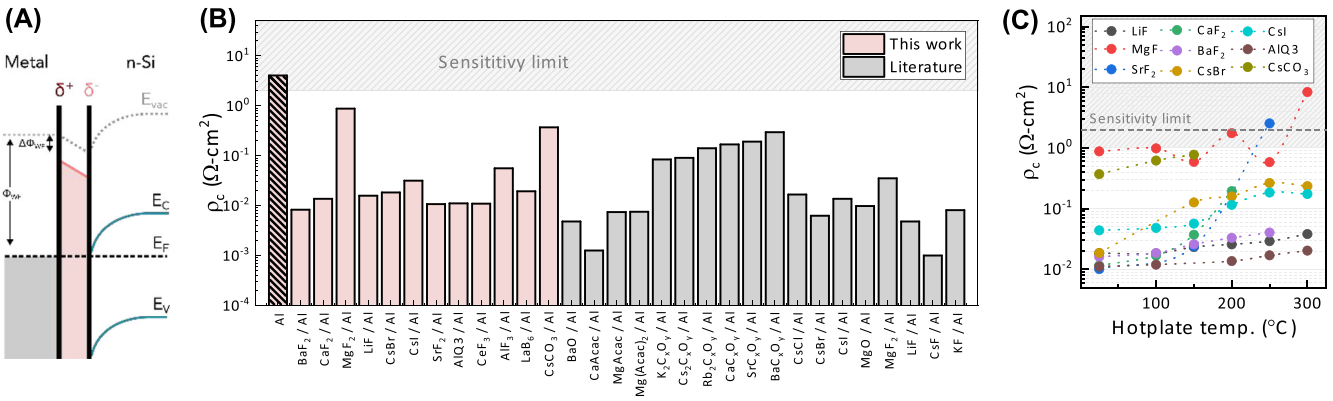

FIGURE 1 (A) Band-diagram schematic showing the downward band bending at the surface of c-Si caused in part by a dipole at the interface. (B) Compilation of different electron contact interlayer materials tested on an n-type c-Si wafer with a moderate resistivity (0.5–2 Ω-cm) taken from our experiments and the literature.[9–11,32–36] The pink and grey bars are those tested in this study and taken from the literature, respectively. All contacts use an Al metal electrode, for reference the hashed bar shows the direct c-Si(n)/Al contact. (C) Temperature-dependence of ρ_c for different materials as an interlayer between c-Si(n) and Al. The shaded area in (B) and (C) indicates the estimated TLM (upper) sensitivity limit using our measurement setup.

area contact on the rear side of a solar cell, permits an efficiency above 20%.

2 | EXPERIMENTAL

All samples for effective minority carrier lifetime (τ_{eff}) and specific contact resistivity (ρ_c) studies were prepared using n-type c-Si substrates with resistivities of 1–3 Ω·cm. These were subjected to a dilute hydrofluoric acid (HF) etch immediately prior to processing. Passivating interlayers were deposited via different techniques. The 2.5–6.5 nm TiO_x films were deposited via a thermal atomic layer deposition (ALD) system (Arradiance GEMStar XT) at a low substrate temperature of 90°C with titanium isopropoxide (TTIP) and water as the precursors. The ~6 nm thick a-Si:H layer was deposited in a plasma-enhanced chemical vapor deposition (PECVD) system. The 2 nm Nb_2O_5 films were deposited via ALD at a deposition temperature of 200°C on top of a SiO_2 interlayer grown via the Radio Corporation of America (RCA) cleaning procedure.[37] More details about this film can be found in reference.[14,38] The ionic films trialed in this study (namely BaF_2, CaF_2, MgF_2, CeF_3, $CsCO_3$, LiF, CsBr, CsI, SrF_2, AlF_3, AlQ_3, and LaB_6) were ~2 nm thick and were thermally evaporated using a tungsten boat (LC Torpedo Glovebox evaporator) at a pressure $<2 \times 10^{-6}$ mbar and a rate of 0.1–0.3 Å/sec. The metal electrodes (~200 nm, unless stated otherwise) were also deposited by thermally evaporating Al at rates of 4–12 Å/sec using the same deposition chamber as the metal compound interlayers without breaking the vacuum. All the annealing treatments mentioned in this study were done using a hotplate in air with a duration of 10 minutes unless otherwise stated.

The samples for ρ_c measurements were made by depositing the ionic and metal layers through a transfer length method (TLM) shadow mask. The current–voltage (I–V) curves were measured using a four-probe configuration to reduce the effect of probe resistance.[39] The τ_{eff} and photoluminescence (PL) samples were made by depositing the passivating interlayer on both sides of the substrates. Using these symmetrical structures, τ_{eff} was extracted as a function of excess minority carrier density Δn using the quasi-steady state photoconductance (QSSPC) method (Sinton Instruments; WCT-120). Since in reality τ_{eff} constitutes a combination of bulk and surface minority carrier lifetime, in this study, we have assumed that the bulk lifetime stays unchanged and thus changes in τ_{eff} are caused only by changes in the surface passivation quality. In the case of the thick metal structures, τ_{eff} was measured as a function of Δn using the quasi-steady-state photoluminescence (QSSPL) technique.[40,41] The reliability of this method was recently validated by a different study.[42] Spectral filters were used to ensure that the collected light is only that of Si band-to-band emission. A further short-pass filter at 1250 nm was added to minimize the impact of rear reflection on the detected signal. Additional information regarding the measurement setup can be found elsewhere.[41,42] In this study, τ_{eff} obtained from both QSSPC and QSSPL is reported at a Δn of 10^{15} cm^{-3}. The PL images were captured using a custom-built PL imaging system.[43] To extract the work function of the contact structure, angle-integrated ultra-violet photoelectron spectroscopy (UPS) measurements were taken using the Helium-I emission spectrum (21.2 eV). For these measurements, the thickness of the Al overlayer was 7 nm. The UPS spectra were obtained in the as-deposited state and after annealing in-situ (in ultra-high vacuum, $<10^{-9}$ mbar) at 250°C for 10 minutes.

The proof-of-concept solar cell was fabricated on a phosphorus-doped (~1 Ω·cm) n-type, float zone, c-Si wafer. Following front surface random pyramid texturing and RCA cleaning, a full-area boron diffusion with a sheet resistance of ~120 Ω/sq was performed in a dedicated clean quartz furnace. The boron-diffused surface was then passivated using a ~18/75 nm AlO_x/SiN_y antireflection stack. The front contacts were photolithographically defined and deposited using thermal evaporation of a Cr (~10 nm)/Pd (~10 nm)/Ag (~100 nm) stack followed by thickening using Ag electroplating. The rear contact was formed by a full-area, 2.5 nm TiO_x film followed by thermal evaporation of a CsBr/Al stack. The light I–V behavior was measured under standard one sun conditions (100 mW cm^{-2}, AM 1.5 spectrum, 25°C) with a 2×2 cm^2 aperture. This setup was calibrated with a certified reference cell (Fraunhofer CalLab).

3 | RESULTS

Figure 1B shows ρ_c values measured for a variety of materials with ionic properties deposited between an n-type c-Si substrate and an Al top electrode. As a reference, a direct c-Si/Al contact is also included as the dashed bar, for which we observed rectifying I–V behavior (in this case ρ_c was approximated as the differential value around 0 V). The bars colored in pink show results from materials tested in this study. It was found that the addition of ~2 nm interlayers produces Ohmic behavior and dramatically improves the contact resistance. Of these interlayers, BaF_2, CaF_2, SrF_2, AlQ_3, AlF_3, and LaB_6 are demonstrated for the first time as Ohmic contacts for n-type c-Si, allowing ρ_c values between 8 and 55 mΩ-cm^2. These results are similar to those already demonstrated in the literature for ionic interlayers of similar thickness,[9–11,32–36] presented as the grey bars in Figure 1B. The temperature dependence of ρ_c for some of the electron contact interlayers from Figure 1B is shown in Figure 1C. Evaluating thermal stability is important since the back-end processing (i.e., encapsulation of solar cells) always involves some annealing steps in a similar temperature regime as the one studied here. Though the general trend is that of an increased ρ_c with increasing temperature, some films show strong degradation whilst others maintain a ρ_c below the 2 Ω-cm^2 resolution limit, in the studied annealing regime. From a ρ_c perspective, the most promising films are CsI, $CsCO_3$, LiF, BaF_2, and CsBr. However, some of these materials exhibited poor air stability, in some cases displaying a visible reaction with air after deposition (e.g., CsI, $CsCO_3$). Additionally, the performance of these interlayers, when incorporated with passivating interlayers, differed significantly. Considering these factors, CsBr was chosen as the best candidate for further study. In this work, we have focused mainly on device performance, and a study of the mechanisms responsible for the

improved performance of CsBr, relative to the other interlayers, will be a topic for future work.

To demonstrate the use of CsBr with different passivation layers, contact resistivity and passivation test structures were fabricated using CsBr/Al contact stacks with three passivating interlayers, a-Si:H, Nb_2O_5, and TiO_x. The measured τ_{eff} for different full-area symmetrical film configurations is shown in Figure 2A in the as-deposited state, after depositing a full-area 2 nm-thick CsBr film, and after the deposition of a 7 nm Al overlayer. Note that the QSSPC measurement cannot be used on a sample with a thick metalization, so a thin Al layer was used in this case, though we acknowledge that the passivation quality with a thicker Al could differ significantly. Firstly, we can observe that CsBr does not provide any passivation when it is deposited directly on c-Si, with and without an Al overlayer. This is likely due to an inability of evaporated CsBr to passivate the vast amount of dangling bonds found at the surface of c-Si, and thus an extra passivating film is required. For thin films of TiO_x, Nb_2O_5, and a-Si:H, a modest level of passivation is provided in the as-deposited state which is unaffected by the thermal sublimation of CsBr on top. Both TiO_x and a-Si:H maintains at least half of the initial τ_{eff} after the thin Al deposition, while for Nb_2O_5, there is a significant degradation after this step. This could be caused by heating during the Al evaporation or by an Al-induced change in the electron-to-hole ratio at the c-Si surface.

A set of accompanying ρ_c test structures was also prepared and is presented in Figure 2B,C. Figure 2B shows the case in which a single interlayer is used between the n-Si and Al, including CsBr, TiO_x, and Nb_2O_5 in direct contact with Al. We have not added data for the a-Si:H/Al contact due to its high contact resistance. It seems that temperatures above 250°C are required to reduce ρ_c of samples that only have a TiO_x or Nb_2O_5 layer below the metal electrode. Figure 2C shows the combined stacks of each of the three passivating interlayers with CsBr/Al. It is clear that the addition of 2 nm CsBr interlayer reduces ρ_c by two orders of magnitude in the case of TiO_x (below 20 mΩ-cm^2) and has also greatly reduced the required annealing temperature for a good contact formation in the case of Nb_2O_5. Conversely, the ρ_c for the a-Si:H interlayer sample starts low in the as-deposited state but increases quickly with the annealing temperature. This behavior in a-Si:H passivating layers is consistent with other studies.[44] Based on the results presented in Figure 2, the TiO_x/CsBr/Al and a-Si:H/CsBr/Al electron contact stacks are taken as the most interesting combinations to test further.

To complement the previous τ_{eff} measurements, the evolution of passivation as a function of the annealing temperature was further studied using PL imaging. PL images of the a-Si:H/CsBr/Al and TiO_x/CsBr/Al (two TiO_x thicknesses of ~2.5 and 6.5 nm) samples were taken after cumulative annealing steps using a hotplate in the air. In these samples, the deposition of CsBr/Al is done through a TLM shadow mask. A thick (~200 nm) Al layer is used to avoid any assumptions regarding the impact of the Al thickness on the extracted parameters. These sets of images are shown in Figure 3A,B. For the a-Si:H case, there is a clear trend in which the surface recombination under the metalized regions (as monitored by the PL counts) is consistently increased with higher annealing temperatures. The increase in PL counts in the non-metalized regions with annealing is likely related to hydrogen diffusing from the as-deposited a-Si:H film into the surface and bulk of c-Si, providing defect passivation.[45] In Figure 3B both TiO_x thicknesses show a similar trend, starting with lower PL counts at the metallized areas as compared to the non-metallized areas. This

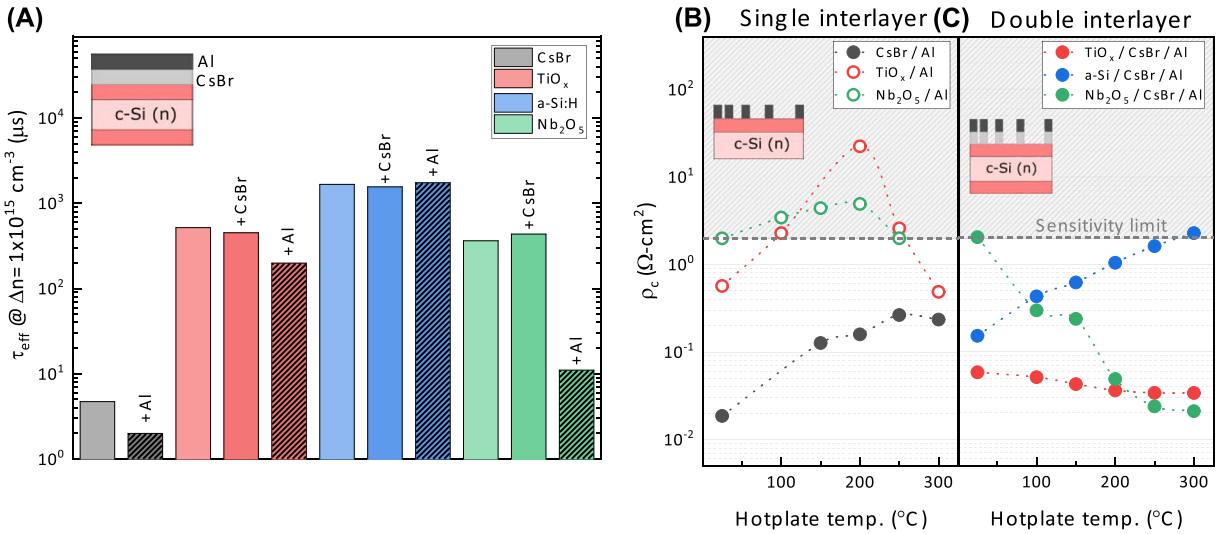

FIGURE 2 (A) Minority carrier lifetime at Δn of 10^{15} cm^{-3} as measured on test structures with symmetrical passivation layers such as TiO_x, a-Si:H, and Nb_2O_5 before and after depositing of CsBr (~2 nm) and Al (~200 nm) layers on one side. The a-Si:H sample was pre-annealed at 200°C for 5 min to obtain a more representative starting value of τ_{eff}. A reference sample without any passivating interlayer (i.e., CsBr/Al directly on c-Si) is also shown. A drawing of these lifetime structures is provided in the inset. (B) Evolution of ρ_c versus annealing temperature for contacts using a single interlayer (either CsBr or a passivating layer without CsBr). (C) ρ_c vs. temperature for samples with a double interlayer (i.e., CsBr on top of a passivating interlayer). The insets in (B) and (C) show schematics of the final TLM devices.

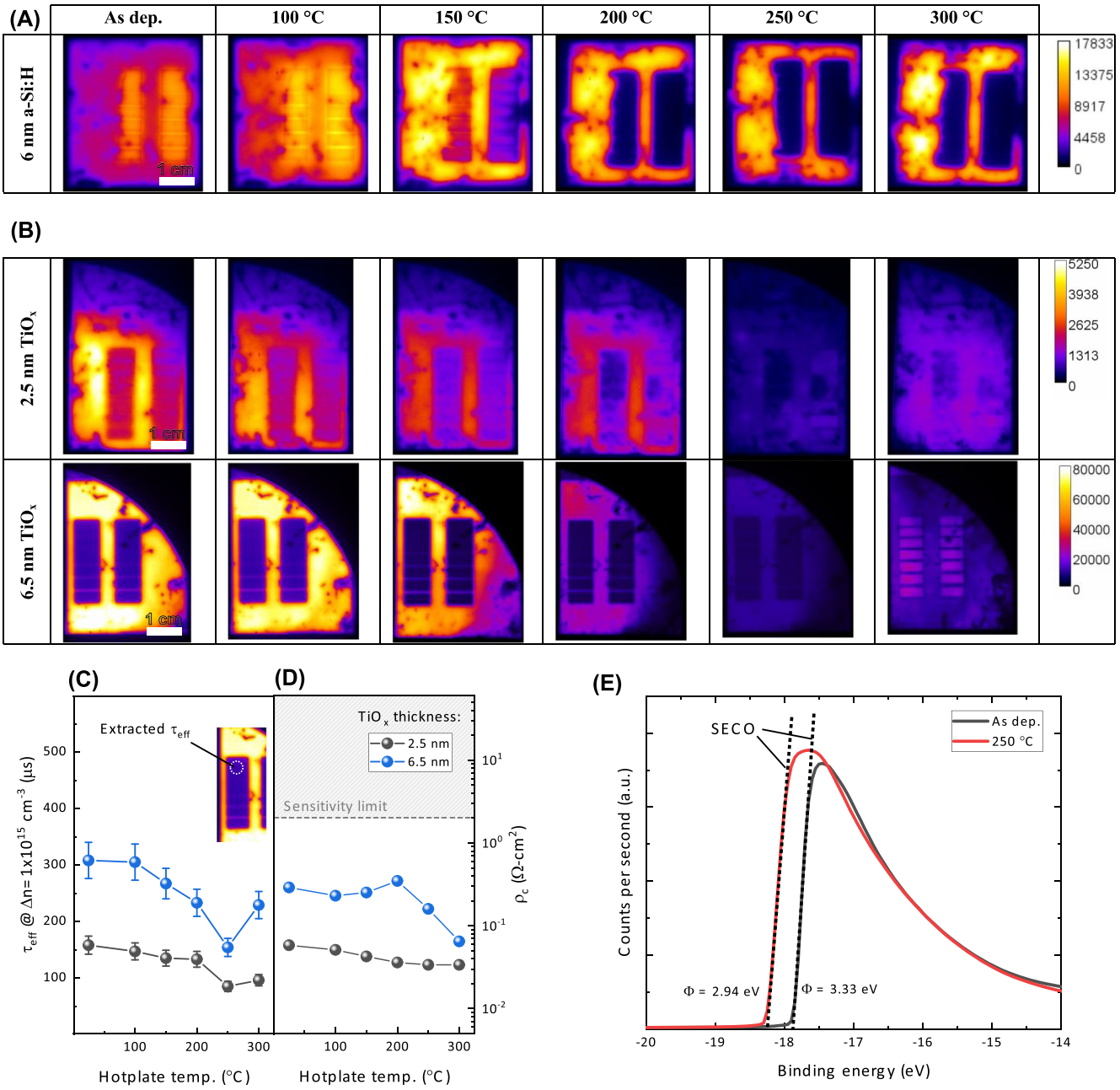

FIGURE 3 (A) PL images for (A) a-Si:H and (B) TiO_x as interlayers between CsBr/Al and n-type c-Si. PL images are taken after sequential annealing steps in air. (C) Effective minority carrier lifetime extracted at the metalized regions in the TiO_x samples and (D) its corresponding ρ_c as measured on sister samples. (E) UPS measurements for a representative TiO_x (2.5 nm)/CsBr (2 nm)/Al (7 nm) sample: as-deposited and in-situ annealed at 250°C. The work function is extracted based on the secondary electron cut-off (SECO), which is shown as dotted lines.

difference between the regions is quantitatively proportional to the decrease in τ_{eff} after the thin (7 nm) Al deposition on the TiO_x/CsBr sample observed in Figure 2A. With increasing temperature, there is minimal change at the metal regions though there is clearly a degradation in the rest of the sample surface, presumably caused by hydrogen effusion and/or crystallization of the TiO_x film. Further annealing reveals that recovery starts to take place for both samples after reaching a temperature above 250°C. This effect is stronger for the thick (6.5 nm) TiO_x sample, where at 300°C the metal regions seem to show better passivation than the non-metalized areas as indicated by a higher PL signal. This interesting behavior was observed in similar PL structures employing Nb_2O_5 instead of TiO_x (not shown). In a more quantitative approach, τ_{eff} at the metallized regions was extracted from the images of Figure 3B at each annealing temperature. These results are depicted in Figure 3C with their accompanying ρ_c values measured on sister samples in Figure 3D. Note that the extracted $\tau_{eff} = 158\,\mu s$ in the as-deposited state for the 2.5 nm TiO_x is lower, but similar to that shown in Figure 2A with a thin Al i.e., $\tau_{eff} = 199\,\mu s$.

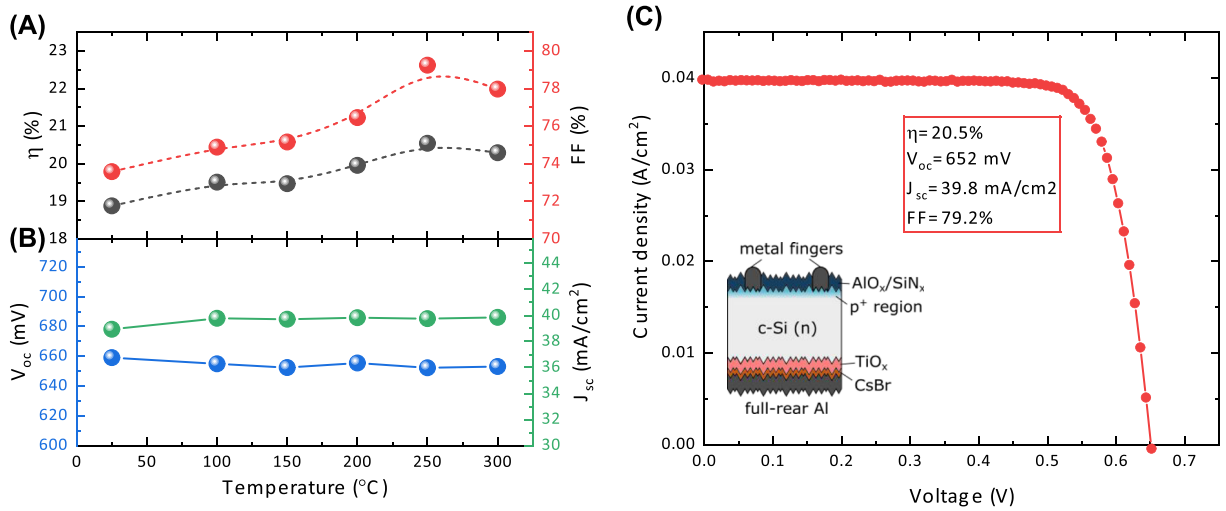

FIGURE 4 (A, B) Evolution of the solar cell parameters as a function of cumulative annealing steps on a hotplate. (C) Current–voltage curve for the condition that yielded the highest efficiency (post-annealing at 250°C). The inset shows a schematic of the front-junction solar cell utilizing a rear full-area TiO_x/CsBr/Al contact.

In general, the trend of Figure 3B is that of a monotonic decrease of τ_{eff} with temperature which is recovered to a small/moderate degree (depending on the TiO_x thickness) at a temperature above 250°C. The ρ_c trend is also very similar for the two samples, where it decreases with increasing temperature. Overall, the 6.5 nm TiO_x provides better surface passivation though this comes at the expense of an increased ρ_c. To investigate the potential origin of the improved contact behavior after annealing, we measured the work function of the n-Si/TiO_x/CsBr/Al sample (using a TiO_x thickness of ~2.5 nm) via He I-UPS secondary electron cut-off (SECO) before and after in-situ annealing in ultra-high vacuum at 250°C for 10 minutes. Note, that the work function is a property of the interface of the sample to the vacuum. This comparison is provided in Figure 3E and shows a decrease in the work function after annealing. In this experiment, the negative shift in the work function could be caused by an increased negative charge concentration (e.g. higher electron concentration at the c-Si surface). Some possible reasons for this include the formation of a strong dipole at the Al/CsBr interface (which could be caused by a Cs+-rich layer at the metal surface), desorption of atmospheric species at the surface of the sample, or reduction of the Al film, which likely partially oxidized during transfer to the UPS chamber.[46–48] These changes observed in the work function, however, are consistent with those observed in the PL images under the assumption that the lower work function electrode creates a higher electron population at the c-Si surface, thus reducing the population of holes and hindering carrier recombination.

Finally, we have employed an electron contact stack of TiO_x (2.5 nm)/CsBr (2 nm)/Al (200 nm) at the rear side of a solar cell. Figure 4A,B shows the evolution of efficiency η, fill factor *FF*, V_{oc}, and short circuit current density J_{sc}, versus temperature (hotplate anneal in air). The increase in efficiency is directly related to an increased *FF*. Though this could correlate to a small degree with the decreased ρ_c observed in the TLM structure, contact sintering at the front side of the cell is likely to play a larger role. We observe that the V_{oc} remains relatively constant at around 650 mV up to 300°C, showing overall good thermal stability which is a requirement for sintering of the front and rear contacts. This also serves as a stability test since similar thermal steps are needed for back-end processing (i.e. encapsulation) when incorporating cells into a module. Figure 4C shows the (inverted) current–voltage curve for the highest efficiency achieved with this device, which reached a value of $\eta = 20.5\%$ after the 250°C annealing step. In terms of the short circuit current J_{sc}, the device shows a value of around 39.8 mA/cm^2, which is consistent with previous studies using a similar fabrication process/structure.[10] Despite the room for improvement in the overall cell design, the TiO_x/CsBr/Al passivating contact stack shows promising behavior and thermal stability for electron contacts.

4 | CONCLUSIONS

In this study, we have shown that many thin (~2 nm) thermally evaporated ionic compound interlayers allow Ohmic contact formation when sandwiched between Al and n-type Si. From this pool of materials, we have focused on CsBr due to its excellent performance when employed with other passivating interlayers, namely a-Si:H, TiO_x, and Nb_2O_5. Based on contact resistivity and effective minority carrier lifetime measurements we found TiO_x/CsBr/Al to be a promising electron contact stack, with a ρ_c < 60 mΩ-cm^2 and a τ_{eff} ~ 200 µs after deposition of a thin Al overlayer. With the aid of PL measurements, we observed a recovery in the passivation quality of the metalized regions in the TiO_x/CsBr/Al stacks after annealing at temperatures above 250°C. This correlated well with work function measurements taken via UPS, where the work function of the sample surface was ~0.3 eV lower after annealing in a vacuum at 250°C. Finally, we demonstrated the potential of the TiO_x/CsBr/Al electron contact stack by

applying it as a full-area rear contact in a solar cell which obtained a cell efficiency above 19% in the as-deposited state and reached an impressive efficiency of ~20.5% after annealing at 250°C. We believe that improvements in this category of electron selective contacts can be achieved by a higher passivation quality of the passivating interlayer used (TiO_x in our case) without compromising ρ_c. Additionally, a more reflective rear stack would be beneficial for the optical performance of the device. This could be achieved by either using a more reflective rear metal (like Ag) or the addition of a transparent conductive oxide which would also enable these wide band gap electron contacts to be used at the front side of solar cell devices.

ACKNOWLEDGEMENTS

This project was supported by the Australian Renewable Energy Agency (ARENA) through project RND013. J.B. acknowledges support from Melbourne Centre for Nanofabrication, through its Technology Fellowship Program. Open access publishing facilitated by The University of Melbourne, as part of the Wiley - The University of Melbourne agreement via the Council of Australian University Librarians.

DATA AVAILABILITY STATEMENT

The data that support the findings of this study are available from the corresponding author upon reasonable request.

ORCID

Anh Huy Tuan Le https://orcid.org/0000-0002-9395-0771
Anyao Liu https://orcid.org/0000-0003-4579-5495
Wenhao Chen https://orcid.org/0000-0002-0360-0373
Bart Macco https://orcid.org/0000-0003-1197-441X
Ziv Hameiri https://orcid.org/0000-0002-2934-4478

REFERENCES

1. Bellini E. JinkoSolar achieves 26.1% efficiency for n-type TOPCon solar cell. 2022.
2. Yoshikawa K, Kawasaki H, Yoshida W, et al. Silicon heterojunction solar cell with interdigitated back contacts for a photoconversion efficiency over 26%. *Nat Energy*. 2017;2(5):17032. doi:10.1038/nenergy.2017.32
3. Haase F, Hollemann C, Schäfer S, et al. Laser contact openings for local poly-Si-metal contacts enabling 26.1%-efficient POLO-IBC solar cells. *Sol Energy Mater sol Cells*. 2018;186:184-193. doi:10.1016/j.solmat.2018.06.020
4. Lin H, Yang M, Ru X, et al. Silicon heterojunction solar cells with up to 26.81% efficiency achieved by electrically optimized nanocrystalline-silicon hole contact layers. *Nat Energy*. 2023;8:1-11.
5. Holman ZC, Descoeudres A, Barraud L, et al. Current losses at the front of silicon heterojunction solar cells. *IEEE J Photovolt*. 2012;2(1):7-15. doi:10.1109/JPHOTOV.2011.2174967
6. Zheng P, Yang J, Wang Z, et al. Detailed loss analysis of 24.8% large-area screen-printed n-type solar cell with polysilicon passivating contact. *Cell Reports Phys Sci*. 2021;2(10):100603.
7. Ibarra Michel J, Dréon J, Boccard M, Bullock J, Macco B. Carrier-selective contacts using metal compounds for crystalline silicon solar cells. *Prog Photovolt*. 2023;31:380-413.
8. Bullock J, Wan Y, Hettick M, et al. Dopant-free partial rear contacts enabling 23% silicon solar cells. *Adv Energy Mater*. 2019;9(9):1803367. doi:10.1002/aenm.201803367
9. Wan Y, Samundsett C, Bullock J, et al. Magnesium fluoride electron-selective contacts for crystalline silicon solar cells. *ACS Appl Mater Interfaces*. 2016;8(23):14671-14677. doi:10.1021/acsami.6b03599
10. Wan Y, Samundsett C, Bullock J, et al. Conductive and stable magnesium oxide electron-selective contacts for efficient silicon solar cells. *Adv Energy Mater*. 2017;7(5):1601863. doi:10.1002/aenm.201601863
11. Bullock J, Hettick M, Geissbühler J, et al. Efficient silicon solar cells with dopant-free asymmetric heterocontacts. *Nat Energy*. 2016;1(3):15031. doi:10.1038/nenergy.2015.31
12. Liu Z, Lin H, Wang Z, et al. Dual functional dopant-free contacts with titanium protecting layer: boosting stability while balancing electron transport and recombination losses. *Adv Sci*. 2022;9(23):e2202240. doi:10.1002/advs.202202240
13. He J, Wang G, Qiu Y, et al. Enabling transparent-conductive-oxide free efficient heterojunction solar cells by flexibly using dopant-free contact. *Adv Funct Mater*. 2022;32(39):2205901. doi:10.1002/adfm.202205901
14. Macco B, Bivour M, Deijkers JH, et al. Effective passivation of silicon surfaces by ultrathin atomic-layer deposited niobium oxide. *Appl Phys Lett*. 2018;112(24):242105. doi:10.1063/1.5029346
15. Wang W, He J, Cai L, et al. Solution-processed electron-selective contacts enabling 21.8% efficiency crystalline silicon solar cells. *Sol RRL*. 2020;4(12):2000569. doi:10.1002/solr.202000569
16. Bullock J, Wan Y, Xu Z, et al. Stable dopant-free asymmetric Heterocontact silicon solar cells with efficiencies above 20%. *ACS Energy Lett*. 2018;3(3):508-513. doi:10.1021/acsenergylett.7b01279
17. Prada S, Martinez U, Pacchioni G. Work function changes induced by deposition of ultrathin dielectric films on metals: a theoretical analysis. *Phys Rev B*. 2008;78(23):235423. doi:10.1103/PhysRevB.78.235423
18. Brabec CJ, Shaheen SE, Winder C, Sariciftci NS, Denk P. Effect of LiF/metal electrodes on the performance of plastic solar cells. *Appl Phys Lett*. 2002;80(7):1288-1290. doi:10.1063/1.1446988
19. Hung LS, Tang CW, Mason MG. Enhanced electron injection in organic electroluminescence devices using an Al/LiF electrode. *Appl Phys Lett*. 1997;70(2):152-154. doi:10.1063/1.118344
20. Ahlswede E, Hanisch J, Powalla M. Comparative study of the influence of LiF, NaF, and KF on the performance of polymer bulk heterojunction solar cells. *Appl Phys Lett*. 2007;90(16):163504. doi:10.1063/1.2723077
21. Hung LS, Zhang RQ, He P, Mason G. Contact formation of LiF/Al cathodes in Alq-based organic light-emitting diodes. *J Phys D Appl Phys*. 2001;35(2):103-107.
22. van Reenen S, Kouijzer S, Janssen RAJ, Wienk MM, Kemerink M. Origin of work function modification by ionic and amine-based interface layers. *Adv Mater Interfaces*. 2014;1(8):1400189. doi:10.1002/admi.201400189
23. Shaheen SE, Jabbour GE, Morrell MM, et al. Bright blue organic light-emitting diode with improved color purity using a LiF/Al cathode. *J Appl Phys*. 1998;84(4):2324-2327. doi:10.1063/1.368299
24. Sun Z, Ding B, Wu B, You Y, Ding X, Hou X. LiF layer at the interface of au cathode in organic light-emitting devices: a nonchemical induced carrier injection enhancement. *J Phys Chem C*. 2012;116(3):2543-2547. doi:10.1021/jp205871a
25. Yeo Y-C, King T-J, Hu C. Metal-dielectric band alignment and its implications for metal gate complementary metal-oxide-semiconductor technology. *J Appl Phys*. 2002;92(12):7266-7271. doi:10.1063/1.1521517
26. Mönch W. On the alleviation of Fermi-level pinning by ultrathin insulator layers in Schottky contacts. *J Appl Phys*. 2012;111(7):073706. doi:10.1063/1.3699180
27. Connelly D, Faulkner C, Clifton PA, Grupp DE. Fermi-level depinning for low-barrier Schottky source/drain transistors. *Appl Phys Lett*. 2006;88(1):012105. doi:10.1063/1.2159096

28. Islam R, Shine G, Saraswat KC. Schottky barrier height reduction for holes by Fermi level depinning using metal/nickel oxide/silicon contacts. *Appl Phys Lett*. 2014;105(18):182103. doi:10.1063/1.4901193
29. Agrawal A, Lin J, Barth M, et al. Fermi level depinning and contact resistivity reduction using a reduced titania interlayer in n-silicon metal-insulator-semiconductor ohmic contacts. *Appl Phys Lett*. 2014; 104(11):112101. doi:10.1063/1.4868302
30. Bagus PS, Staemmler V, Wöll C. Exchangelike effects for closed-Shell adsorbates: interface dipole and work function. *Phys Rev Lett*. 2002; 89(9):096104. doi:10.1103/PhysRevLett.89.096104
31. Cuevas A, Wan Y, Yan D, et al. Carrier population control and surface passivation in solar cells. *Sol Energy Mater sol Cells*. 2018;184:38-47. doi:10.1016/j.solmat.2018.04.026
32. Kim S-H, Jung J-Y, Wehrspohn RB, Lee J-H. All-room-temperature processed 17.25%-crystalline silicon solar cell. *ACS Appl Energy Mater*. 2020;3(4):3180-3185. doi:10.1021/acsaem.0c00133
33. He J, Wang W, Cai L, et al. Stable electron-selective contacts for crystalline silicon solar cells enabling efficiency over 21.6%. *Adv Funct Mater*. 2020;30(50):2005554. doi:10.1002/adfm.202005554
34. Yao Z, Cai L, Meng L, et al. High-performance and stable dopant-free silicon solar cells with magnesium acetylacetonate electron-selective contacts. *Phys Status Solidi RRL*. 2020;14(6):2000103. doi:10.1002/pssr.202000103
35. Wan Y, Bullock J, Hettick M, et al. Temperature and humidity stable alkali/alkaline-earth metal carbonates as electron heterocontacts for silicon photovoltaics. *Adv Energy Mater*. 2018;8(22):1800743. doi:10.1002/aenm.201800743
36. Wang W, He J, Cai L, et al. Solution-processed electron-selective contacts enabling 21.8% efficiency crystalline silicon solar cells. *Solar RRL*. 2020;4:2000569.
37. Itano M, Kern FW, Miyashita M, Ohmi T. Particle removal from silicon wafer surface in wet cleaning process. *IEEE Trans Semicond Manuf*. 1993;6(3):258-267. doi:10.1109/66.238174
38. Macco B, Black LE, Melskens J, et al. Atomic-layer deposited Nb2O5 as transparent passivating electron contact for c-Si solar cells. *Sol Energy Mater sol Cells*. 2018;184:98-104. doi:10.1016/j.solmat.2018.04.037
39. Schroder DK. Resistivity. In: *Semiconductor Material and Device Characterization*. John Wiley & Sons, Ltd; 2005:1-59.
40. Dumbrell R, Juhl MK, Li M, Trupke T, Hameiri Z. Metal induced contact recombination measured by quasi-steady-state photoluminescence. *2017 IEEE 44th Photovoltaic Specialist Conference (PVSC)*. 2017:3315–3318.
41. Dumbrell R, Juhl MK, Trupke T, Hameiri Z. Extracting metal contact recombination parameters from effective lifetime data. *IEEE J Photovolt*. 2018;8(6):1413-1420. doi:10.1109/JPHOTOV.2018.2861761
42. Le AHT, Bonilla RS, Black LE, et al. Recombination in passivating contacts: investigation into the impact of the contact work function on the obtained passivation. *Solar RRL*. 2023;7(11):2201050. doi:10.1002/solr.202201050
43. Nie S, Kristensen ST, Gu A, Chin RL, Trupke T, Hameiri Z. Photoluminescence-based spatially resolved temperature coefficient maps of silicon wafers and solar cells. *IEEE J Photovolt*. 2020;10(2):585-594. doi:10.1109/JPHOTOV.2019.2956261
44. Luderer C, Messmer C, Hermle M, Bivour M. Transport losses at the TCO/a-Si:H/c-Si heterojunction: influence of different layers and annealing. *IEEE J Photovolt*. 2020;10(4):952-958. doi:10.1109/JPHOTOV.2020.2983989
45. Yang HJ, Ji K, Choi J, Lee HM. Annealing effect on surface passivation of a-Si:H/c-Si interface in terms of crystalline volume fraction. *Curr Appl Phys*. 2010;10(3):S375-S378. doi:10.1016/j.cap.2010.02.055
46. Semov YI. Work function of oxidized metal surfaces and estimation of Al_2O_3 film band structure parameters. *Physica Stat Solidi (b)*. 1969; 32(1):K41-K44. doi:10.1002/pssb.19690320162
47. Cornette P, Costa D, Marcus P. Relation between surface composition and electronic properties of native oxide films on an aluminium-copper alloy studied by DFT. *J Electrochem Soc*. 2020;167(16): 161501. doi:10.1149/1945-7111/abc9a1
48. Halliday MT, Hess WP, Shluger AL. A mechanism of Cu work function reduction in CsBr/Cu photocathodes. *Phys Chem Chem Phys*. 2016; 18(10):7427-7434. doi:10.1039/C5CP07694C

How to cite this article: Michel JI, Le AHT, Yan D, et al. Electron contact interlayers for low-temperature-processed crystalline silicon solar cells. *Prog Photovolt Res Appl*. 2025; 33(9):927-934. doi:10.1002/pip.3768